High Wear Resistance and Mechanical Performance of NiAl Bronze Developed by Electron Beam Powder Bed Fusion

Wenzheng Zhai[1], Aidong Sun[1], Wenhan Zeng[2], Wenlong Lu[1], Xiaojun Liu[1], Liping Zhou[1], Jian Wang[1], Ahmed Mohamed Mahmoud Ibrahim[3]

Abstract

This work reports the additively manufactured NiAl bronze alloys via electron beam powder bed fusion (EB-PBF) that exhibit improved wear resistance without an increase of friction, exceeding those of conventional hot-rolled counterparts. High wear resistance is attributed to the formation of a Cu–O-rich transfer layer, and to exceptional mechanical strength induced by integrated effects including uniformly distributed precipitation, grain refinement, martensitic transformation around stacking faults, and a modulus mismatch between precipitates and the matrix. The simulation results indicate that the effect of the precipitate distribution on the internal stress field of the matrix is dependent on the external force direction. For the shear force, the uniformly distributed precipitates promote the overall stress concentration of the matrix, leading to its high work-hardening capability that plays a role in improving the wear resistance. This study reveals the potential of the EB-PBF technique to develop alloys with high wear resistance.

Keywords Fretting · Metal-matrix composite · Additive manufacturing · Electron microscopy · Finite element modelling

1 Introduction

A good combination of high strength and good corrosion resistance of NiAl bronze (NAB) alloys enables them to be used in a variety of engineering applications such as gears, dies, bushings, and guide plates [1], where high resistance to wear is desirable. By appropriate treatments including equal channel angular extrusion [1, 2], laser surface melting [3, 4], and friction stir processing [5, 6], an enhancement of the strength and the wear resistance can be obtained which is attributed to the grain refinement. While these techniques are normally effective for a geometry that is easy to machining, advanced methods for the improvement of wear resistance are required which can enable the geometry required for best performance from restrictions imposed by traditional machining.

Recently, additive manufacturing (AM) shows great potential in producing metallic materials with tailored microstructures and superior mechanical properties compared to traditional manufacturing processes [4, 7–14]. However, the difficulty remains for manufacturing dense parts of Cu-based alloys through the AM due to their high reflectivity against infrared laser [15–17]. Several copper-based components have been fabricated by the AM including 99.8 wt% Cu–O [18], Cu-(0.5–0.7)Cr-(0.02–0.05)Zr-(0.02–0.05) Ti (wt%) [19] and C11000 copper [20] alloys, but great challenges still exist for producing them with fine-grained microstructures and required mechanical properties. The Cu–Cr–Zr–Ti alloys fabricated by the selective laser melting consisted of relatively coarse grains with sizes ranging from 30 to 250 μm, and showed a relative density of 97.9%, resulting in the lower ultimate tensile strength (~ 20 to 25%) compared to the hot-rolled counterparts [19]. Sciammarella et al. [20] deposited copper powders onto the 4142 steel surface using the laser beam melting to fabricate the pure copper with the grain size of 20 μm, which was smaller than that of hot-rolled copper materials. Recently, Liu et al. [21] built NAB thin wall sample by the laser melting deposition technique. The built samples showed ultimate tensile strength values of 645 ± 5.7 MPa and 637 ± 9.9 MPa along the scanning and deposition directions, respectively. Nevertheless, the AM-processed copper showed a low hardness compared to the hot-rolled counterpart. Hence, more efforts should be devoted to develop AM Cu-based alloys so as to provide high performance materials with controllable microstructures [22]. Considering high reflectivity of Cu and its alloys against infrared laser (1060 nm wavelength),

[1] School of Mechanical Science and Engineering, Huazhong University of Science and Technology, Wuhan 430074, People's Republic of China

[2] The EPSRC Future Metrology Hub, University of Huddersfield, Huddersfield HD13DH, UK

[3] Department of Production and Design Engineering, Minia University, Minya 61519, Egypt

which is the predominant energy source in the L-PBF technique [9], the electron beam powder bed fusion (EB-PBF) method was selected to build NAB alloys. Moreover, the wear resistance of AM Cu-based alloys fabricated by EB-PBF remains unknown.

Wear performance of NAB is critical for controllable pitch propellers where fretting wear commonly occurs with a form of flat-on-flat contact between the blade carrier and the hub [23]. In this work, NAB alloys are successfully fabricated by the EB-PBF technique. Their tribological and mechanical properties are evaluated by fretting wear and tensile tests. The tribological and mechanical behaviors of conventional hot-rolled counterparts are examined for comparison. Wear resistance mechanisms of the EB-PBF materials are obtained by the transmission electron microscope (TEM) and finite-element (FE) modeling. The effect of the precipitate distribution in terms of uniform and non-uniform on the stress field of the matrix is analyzed.

2 Experimental Details

2.1 Fabrication of Materials

In this work, specimens were prepared from the gas atomized NAB alloy powders with the composition of $Cu_{81.1}Al_{9.5}Ni_{4.2}Fe_4Mn_{1.2}$ by an EB-PBF 250 system (Qbeam3D) with following optimized parameters: a scanning speed of 1 m/s, a hatch distance of 150 μm, beam currents of 7 mA. The powder diameter ranges from 63 to 105 μm. Each layer was scanned twice using vectors oriented along scan directions x and y, alternatively. Before the EB-PBF process, the stainless steel plate was preheated with a scanning speed of 15 m/s and a beam current of 15 mA for 9 s. Each powder layer was also preheated by beam scanning at a line rate of 2 m/s and a beam current of 5 mA, which could reduce thermal stresses of materials during the AM process. Based on the Archimedes method, the relative density of built samples was 99.9 ± 0.03%.

2.2 Tribological and Mechanical Tests

In practical applications of controllable pitch propellers, materials for the hub and the blade carrier are NAB
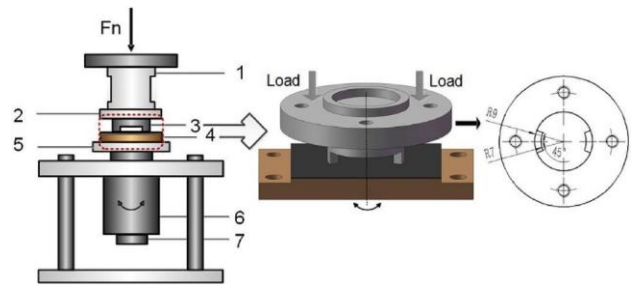
Fig. 1 Schematic of tribosystem with the flat-on-flat configuration. 1:torque sensor; 2: upper holder; 3:counterpart; 4: sample; 5: Lower holder; 6:stepping motor; 7: encoder [29]

alloys and 42CrMo4, respectively. To characterize the wear behavior, torsional fretting wear tests were carried out using the flat-on-flat configuration at contact loading ranging from 43 to 106 N (corresponding to contact pressure of 1.52–3.75 MPa) and with a frequency of 2 Hz for 2×10^4 cycles. The counterpart material was 42CrMo4 steel, which has a hardness of 270 HV and a roughness of R_a = 0.2 μm. Specific mechanical properties of 42CrMo4 steel used in this study are listed in Table 1. As depicted in our previous works [24–28], the samples were fixed on the lower holder that is driven by a reduced speed stepping motor with a rotational angle resolution of 0.018°, Fig. 1. The counterpart is fixed on the upper holder, which is connected with a torque sensor. Normal loading is applied by static loads from the top. The angular displacement, frequency and fretting cycles of the samples are controlled by the motor impulse and recorded by an encoder. Mechanical properties were evaluated by rate-controlled tensile tests under a strain rate of 1.0×10^{-3} s^{-1} via the Shimadzu AG100KN device equipped with a non-contact laser extensometer to obtain the strain. During tensile testing, two pieces of copper tape acting as reflective markers for the extensometer were attached to the sample gauge. Non-proportional samples were designed for tensile tests. The tensile testing was conducted according to ASTM E 8 M. All test samples were processed from the EB-PBF materials by wire cutting with the size of 2.0 mm in width, 1.8 mm in thickness, and 6.0 mm in gage length. The tribological and mechanical tests were repeated three and six times for each specimen, respectively, yielding standard error bars. The Vickers hardness of the specimens was determined based on the standard ASTM-E92-82 using an HVS-1000 Vickers hardness device.

2.3 Finite-Element (FE) Modeling

An FE model for the evaluation of the stresses of uniform and non-uniform precipitate specimens during the friction

Table 1 Mechanical properties of the 42CrMo4 counterpart

Material	Hardness (HV)	Yield strength (MPa)	Tensile strength (MPa)	Elasticity modulus (GPa)	Poisson's ratio
42CrMo4	270	550	800	212	0.3

process was built using the finite-element technique. A commercially available FE package (ANSYS) was used to estimate the effect of precipitate distributions within the matrix. Two different geometries with the element mesh applied in the simulations were defined, representing the matrix and the precipitate, respectively. On the basis of the experimental results, the same volume fraction of 26.4% was used in the simulation of both uniform and non-uniform precipitation samples. During the modeling, the bottom interface of the samples was kept fixed, while the top interface of the samples and their circumferential surfaces were maintained as free. Additionally, the shear force of 3.75 MPa obtained from the tribological test was applied. Mechanical properties of the matrix and the precipitate applied in the simulation are listed in Table 2, which were based on the experimental characterization. Detailed information to obtain the mechanical properties can found in our previous study [30].

2.4 Microstructural Characterizations

The microstructures of bulk samples were investigated by a JSM-7600F field emission scanning electron microscopy (FE-SEM) and a JEOL JEM 2100 TEM. To determine the precipitate distribution, electrolyte polishing and etching were conducted on the NAB specimens with a solution of 10 g $FeCl_3$ + 30 mL HCl + 160 mL H_2O at 25 ℃. Morphologies of wear surfaces were characterized by the optical microscope (OM, OLYMPUS DSX510 3D) and the FE-SEM. The specimen for electron backscatter diffraction (EBSD) characterization was mechanically polished down to 0.05 μm diamond suspension, followed by vibration polishing of 6 h to reduce the residual deformation. EBSD was carried out by a field emission gun scanning electron microscope (FEI Inspect F50 FEG SEM) at 20 kV with a step size of 0.24 μm. Focused ion beam (FIB) was performed on the wear surfaces of EB-PBF C63000 alloys and 42CrMo4 to observe microstructures of the subsurface. Wear surfaces of the 42CrMo4 counterbodies for EB-PBF and hot-rolled samples at the contact load of 106 N were characterized by FE-SEM and energy disperse spectroscopy (EDS).

3 Results

The strain can be accommodated more readily in a fine equiaxed structure [31]. However, producing an ideal equiaxed structure requires large amounts of undercooling, which has proven difficult in AM process [32]. In this study,

Table 2 Mechanical properties of the matrix and the precipitate applied in the FE model

double scanning for each layer proves to be effective to provide adequate processing paths for producing fine equiaxed grains. EBSD characterization, shown in Fig. 2a, presents microstructures of the NAB alloy, indicating that an equiaxed grain size of 16 ± 4.2 μm is obtained by EBPBF, which is decreased compared to the reported AM Cu-based alloys (20–250 μm) [18, 19]. Figure 2b presents SEM images of the deep etched microstructures, in which homogeneously distributed precipitates are exposed. The high magnification image for the EB-PBF-processed alloy (inset in Fig. 2b) clearly shows that the grains are highly decorated by non-coherent intragranular precipitates, which will contribute to the strength by the Orowan by-passing mechanism. The precipitates are also clearly observed in the TEM image (Fig. 2c). The lamellar structure, indicated by an arrow in Fig. 2c, is determined as the B2-NiAl phase, and the elliptical phase (indicated by a circle) corresponds to the ordered Fe_3Al phase, with their selected-area electron diffraction (SAED) patterns given in Fig. 2d and e. In addition to the present precipitates, several SFs showing straight streaks are found in TEM bright- and dark-field micrographs of the EB-PBF-processed NAB alloy, and terminate inside the grains with bright and dark contrast, as shown in Fig. 2f and g. High-density dislocations are also observed around the SFs, implying that the SFs may originate from rungs with a high dislocation density [33]. Figure 2h presents the high-resolution transmission electron microscopy (HRTEM) image of the SFs which are identified as on the (1 1 1) plane. Moreover, the SFs in Fig. 2h are decorated by several dark speckles, which are the footprints of dislocations interacting with the SFs. The dislocation-SF interaction was also observed by Agnew et al. [34] and Li et al. [35]. Table 3 gives the comparison of mechanical properties and wear behaviors between the EB-PBF specimens and the most common hot-rolled NAB materials. The NAB alloy has a hardness of 240 ± 15 HV, resulting from the high precipitation content of Fe_3Al and NiAl. The yield strength is around 380 MPa combined with a tensile strength of ~950 MPa (Fig. 3), which is much higher than the most common hotrolled NAB material (Table 3). Such high strengths are resulted from the grain refinement through the Hall–Petch relationship and the precipitate strengthening by the Orowan looping mechanism. Besides the attractive mechanical behavior, the EB-PBF samples show a significantly higher wear resistance compared to the hot-rolled NAB samples at the given test conditions.

	Matrix	Precipitate
Elastic modulus	110 GPa	140 GPa
Shear modulus	40 GPa	87 GPa
Poisson ratio	0.31	0.33
Density	8.9 g/cm^3	6.53 g/cm^3
Yield strength	220 MPa	386 MPa
Grain size	16 μm	410 nm
Volume fraction	/	26.4%

Fig. 2 a EBSD observation of microstructures of NAB alloys with quasi-equiaxed grains; **b** SEM image of the deep etched microstructures with homogeneously distributed precipitates, the inset indicates that the grains are highly decorated by non-coherent intragranular precipitates; **c** TEM image of intragranular precipitates, the inset is the SAED pattern of the Cu matrix; **d, e** SAED patterns of Fe$_3$Al and NiAl precipitates, respectively; **f, g** TEM bright- and dark-field micrographs of the NAB alloy, showing SFs with straight streaks; **h** HRTEM image of SFs on the (111) plane
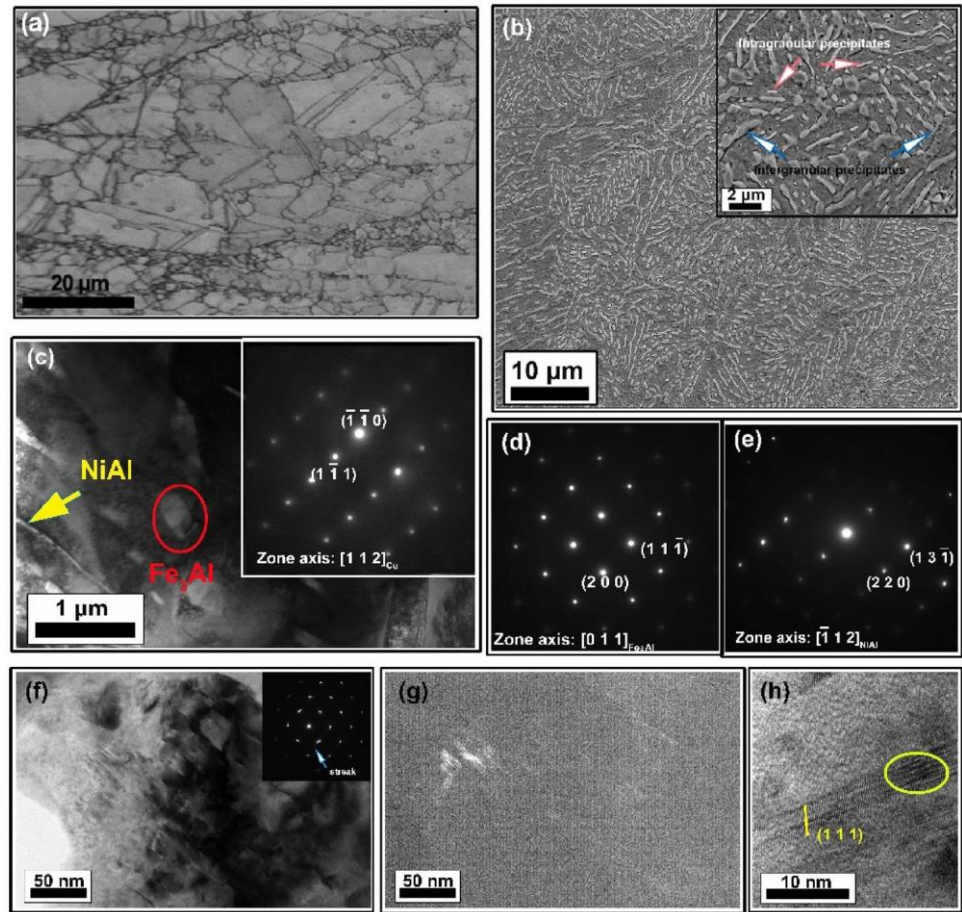
Table 3 Comparison of wear behaviors and mechanical properties between the EB-PBF specimens and the most common hot-rolled NAB materials

Material	Wear (× 10^7 μm^3)			Hardness (HV)	Yield strength (MPa)	Tensile strength (MPa)	Elongation (%)
	43 N	86 N	106 N				
Hot-rolled NAB	6.7 ± 0.3	14.6 ± 0.7	24.5 ± 1.0	200 ± 22	295 ± 17	635 ± 19	17
EB-PBF NAB	2.1 ± 0.4	3.9 ± 0.2	9.8 ±0.7	240 ± 15	382 ± 22	950 ± 28	34.1 ± 1.1

The considerably higher wear resistance of EB-PBF C63000 is likely related to its sustainable work-hardening ability. The work-hardening effect plays an important role in the wear resistance due to precipitates or second phases that hinder the dislocation motion [36]. Figure 4a gives work-hardening rates for EB-PBF and hot-rolled C63000

materials. The work-hardening rate of EB-PBF materials is considerably higher than that of hot-rolled counterparts at strains above 0.09. It consequently results in surface hardening during the fretting wear process, characterizing decreased wear rate. This is consistent with the superior wear resistance of the EB-PBF C63000 materials.

Figure 4b shows the friction coefficients of the EB-PBF and hot-rolled C63000 materials at the contact load of 106 N. While the wear resistance of the EB-PBF C63000 materials is significantly improved, interestingly, the friction coefficient of EB-PBF C63000 remains at ~ 0.4 that is comparable to that of hot-rolled materials. Additionally, the friction coefficient of EB-PBF C63000 is more stable over
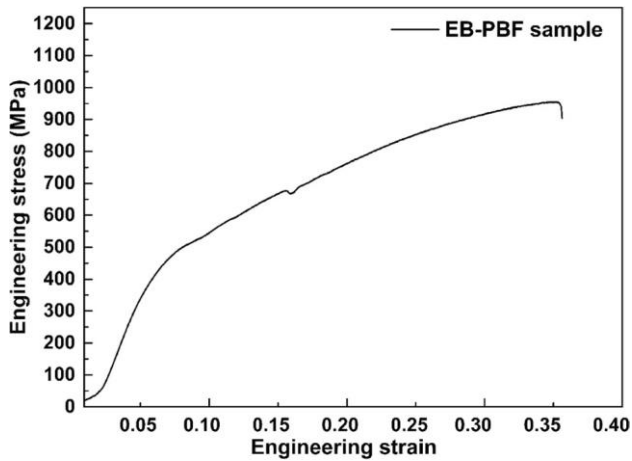

Fig. 3 Tensile stress–strain curve of the EB-PBF specimen

that of the hot-rolled counterpart, which can be attributed to less wear debris within the interface of the friction pair during fretting.

Figure 5 presents 3D height mappings and SEM images of the wear surfaces of EB-PBF samples after wear tests under 43, 86 and 106 N. Mild wear is observed for EB-PBF samples at each test condition, indicated by red quadrilateral as shown in Fig. 5a–c. Further microstructural characterization by SEM shows the shallow discontinuous scratches for the wear surfaces (Fig. 5d–f), indicating the dominant abrasive wear mechanism during fretting. The wear mechanism of the wear surfaces is strongly influenced by the hardness and microstructures of the

tested materials. With an increased hardness and a high content of precipitates, a decreased penetration depth on the wear surfaces by asperities of the 42CrMo4 counterpart can be observed, resulting in slight material damage. A high magnification image for the wear surface tested at 106 N clearly shows a uniform distribution of precipitates after fretting wear. Our previous work has demonstrated that precipitates had a significant effect on the improvement of the wear resistance of NAB alloys under fretting conditions [24]. The significantly improved wear resistance is attributed to (i) reduction of the local stress level around the crack tip owning to the high elastic modulus mismatch between the NiAl precipitate and the matrix; (ii) and crack extension toughening effect at the interface of the matrix and the precipitate induced by their high plastic mismatch.

Figure 6 gives the FE-SEM image of the cross section of the EB-PBF sample after wear at 106 N to observe subsurface microstructures. Microploughing can be observed (Fig. 6a). From the EDS result of the top surface of the cross section (Fig. 6b), a high content of element O indicates triboxidation would be occurred during the wear process.

Since the SFs combined with a high density of dislocation have been observed in the EB-PBF alloys (Fig. 2f), other possible effects such as dislocation-SF interactions may also play an important role in wear resistance. Extremely fine structures with random crystallographic orientations are found in the subsurface of the EB-PBF sample after wear tests (Fig. 7a). The wear resistance is likely to change when the grain size is reduced from the micron scale to the nanoscale [37]. In addition, typical deformation microstructures with fine martensite plates are formed (Fig. 7b), indicating a strain-induced martensitic transformation during fretting wear. The formation of martensite grains suggests that the microstructure of the EB-PBF NAB alloy with a high content of SFs and dislocations is unstable under the cyclic shear stress. The transformation of martensite can provide high hardness but may cause embrittlement subjected to high strains [38]. Since fretting normally occurs with small amplitude oscillatory displacement between surfaces in contact, such martensitic transformation is an effective way to improve the wear resistance. Interestingly, this amount of
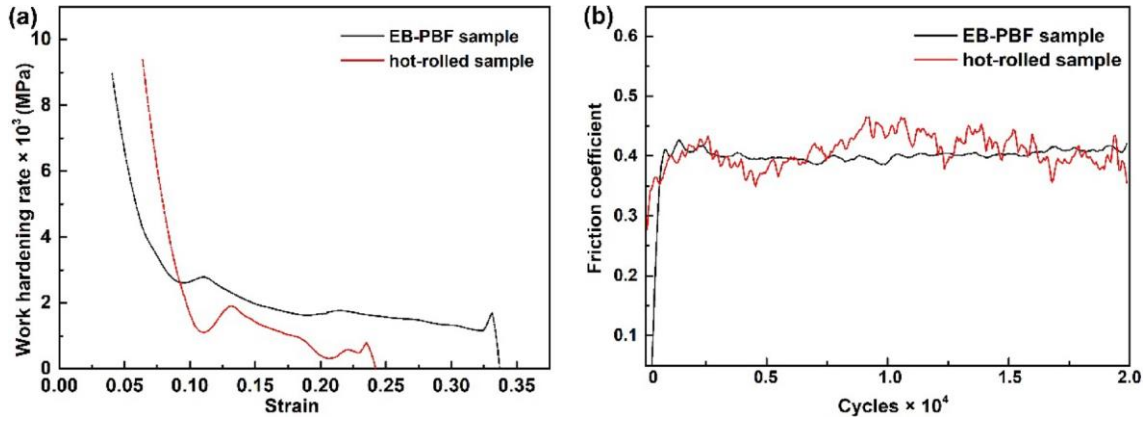
Fig. 4 **a** Work-hardening rate versus true strain curves and **b** friction coefficient results at the contact load of 106 N of EB-PBF materials and the hot-rolled C63000
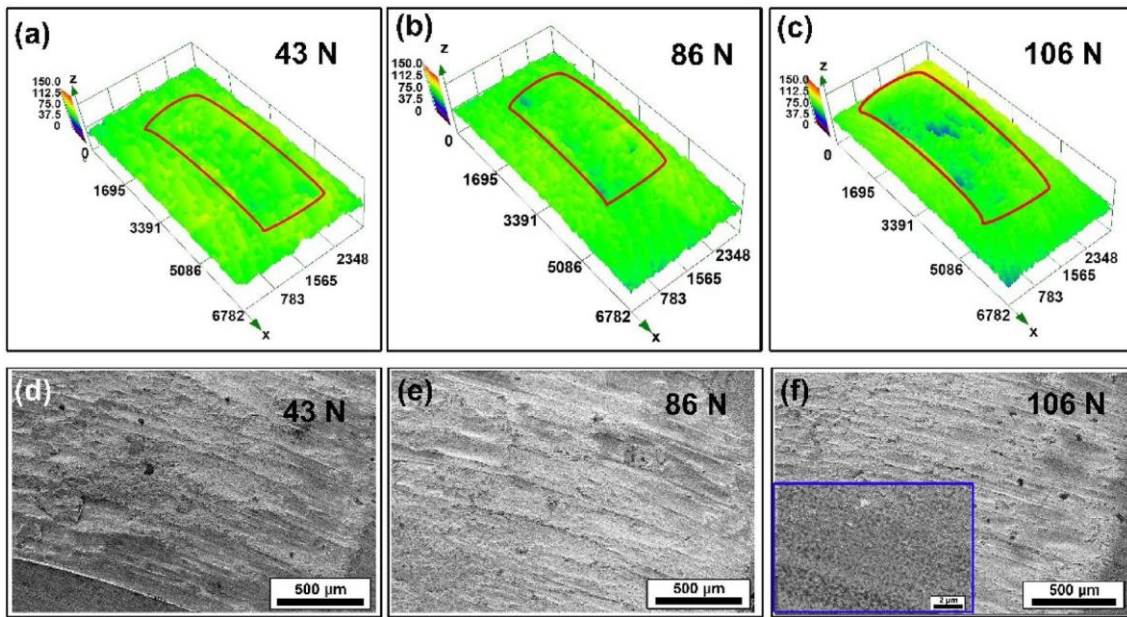

Fig. 5 **a–c** 3D height mappings and **d–f** SEM images of the wear surfaces of EB-PBF samples after wear tests under 43, 86, and 106 N
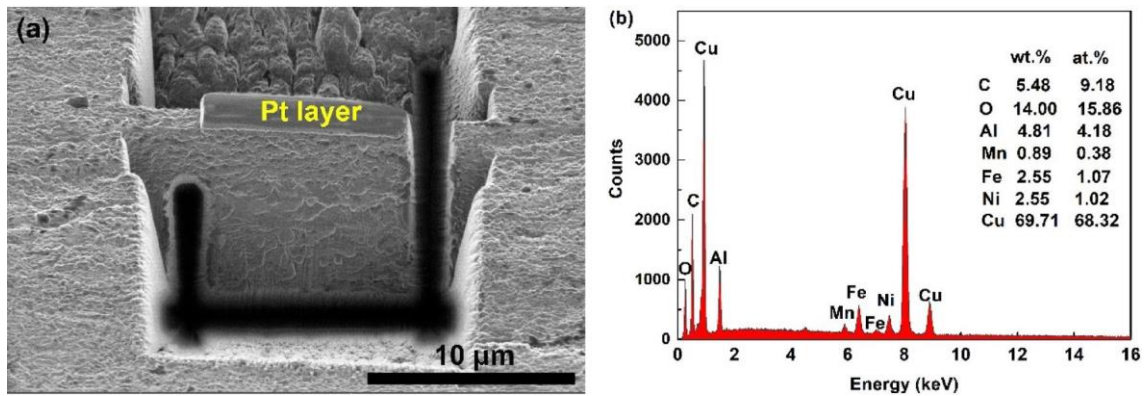

Fig. 6 **a** A top-side view of the cross section of the EB-PBF alloy after wear at 106 N, **b** the EDS result of the top surface of the cross section

Fig. 7 TEM observations of **a** extremely fine structures of the subsurface with random crystallographic orientations after wear tests; **b** deformation microstructures with fine martensite plates; **c** martensite preferentially appears at the SF bands; **d** high magnification TEM image for the rectangular area in image **c**; **e**–**g** change of crystal structures from the fcc phase to the bcc martensite phase
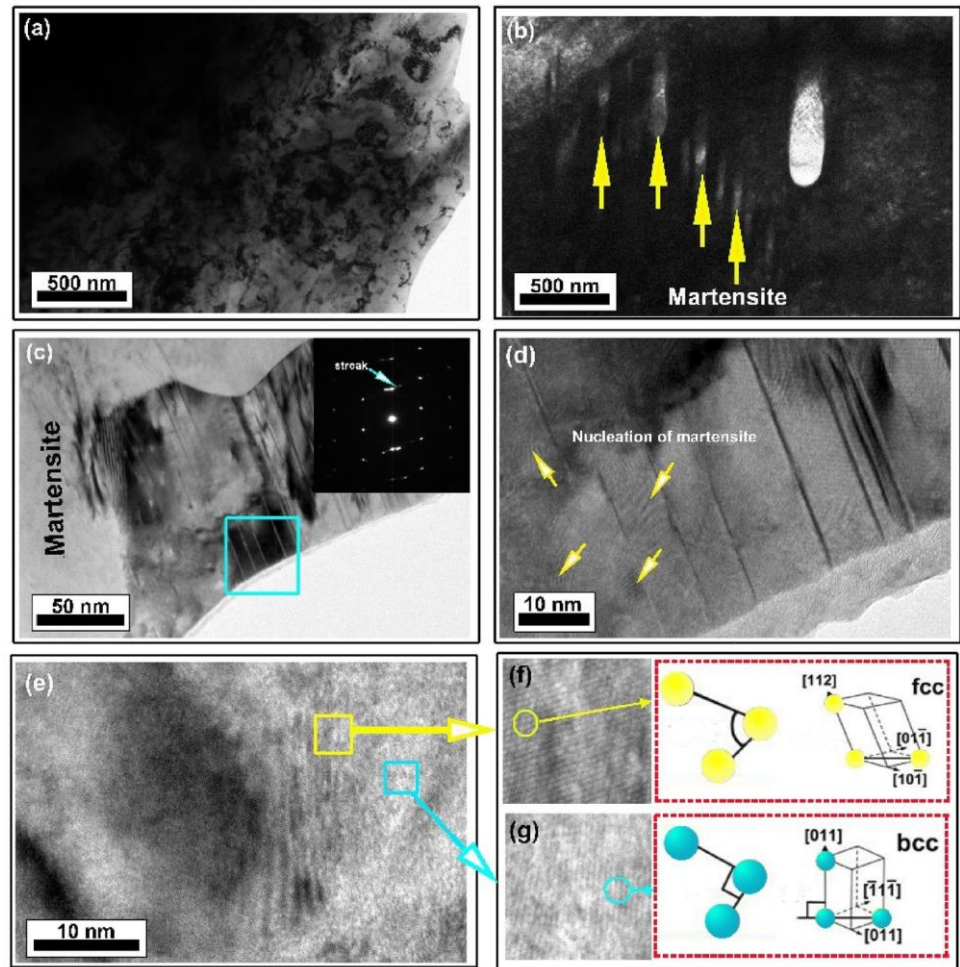
martensite is found to preferentially appear at the SF bands (Fig. 7c), confirmed by the strain-induced nucleation of martensitic transformations around the SFs (Fig. 7d). Figure 7e–g provide the evidence of the collective movement of atoms at the atomic scale, resulting in the change of crystal structures from the fcc phase to the bcc martensite phase. This observation is in good agreement with the simulation result for martensitic transformations [39, 40].

The EB-PBF parts show improved wear behavior. It is critical to understand whether the counterbodies suffer from increased wear for the better tribological behavior of the EBPBF parts. The results of wear weights of the counterbodies for both EB-PBF and hot-rolled samples are negligible, which may result from the higher hardness of 42CrMo4 than that of EB-PBF and hot-rolled NAB alloys. Figure 7 shows the wear surfaces of the 42CrMo4 counterbodies for EBPBF and hot-rolled samples at the contact load of 106 N. Slight scratches with the material transfer are observed on the surface of 42CrMo4 counterbodies (Fig. 8a, b). A high magnification of the wear morphology of the 42CrMo4 counterbody for the EB-PBF

sample demonstrates a compact transfer layer (Fig. 8c). The EDS analysis of the compact transfer layer shows Cu-element enrichment, indicating surface materials transfer from the NAB to the 42CrMo4 counterbody. Additionally, a high content of element O in the transfer layer reveals oxidation and mechanical mixing in the layer, which is consistent with the EDS analysis of the wear subsurface of the EB-PBF sample (Fig. 6b). The transfer layer can protect the contact surface from direct wear, promoting tribological behavior.

To further observe the subsurface microstructure of the 42CrMo4 counterbody, a SEM lamella of its surface and subsurface was obtained from the transfer layer position via FIB. Figure 9a presents the top view of an ion-induced secondary electron image of the lamella position, where the lamella was cut into the 42CrMo4 substrate after coating a Pt layer. Figure 9b shows the SEM image of the cross-section of the wear surface. A thin transfer layer with a thickness of ~ 0.9 μm is observed. No crack or deformation can be found in the substrate. No sign of wear is consistent with the result of negligible wear weight. The

transfer layer on the wear surface could reduce the shear stress at the contact interface and thus hinder surface wear.
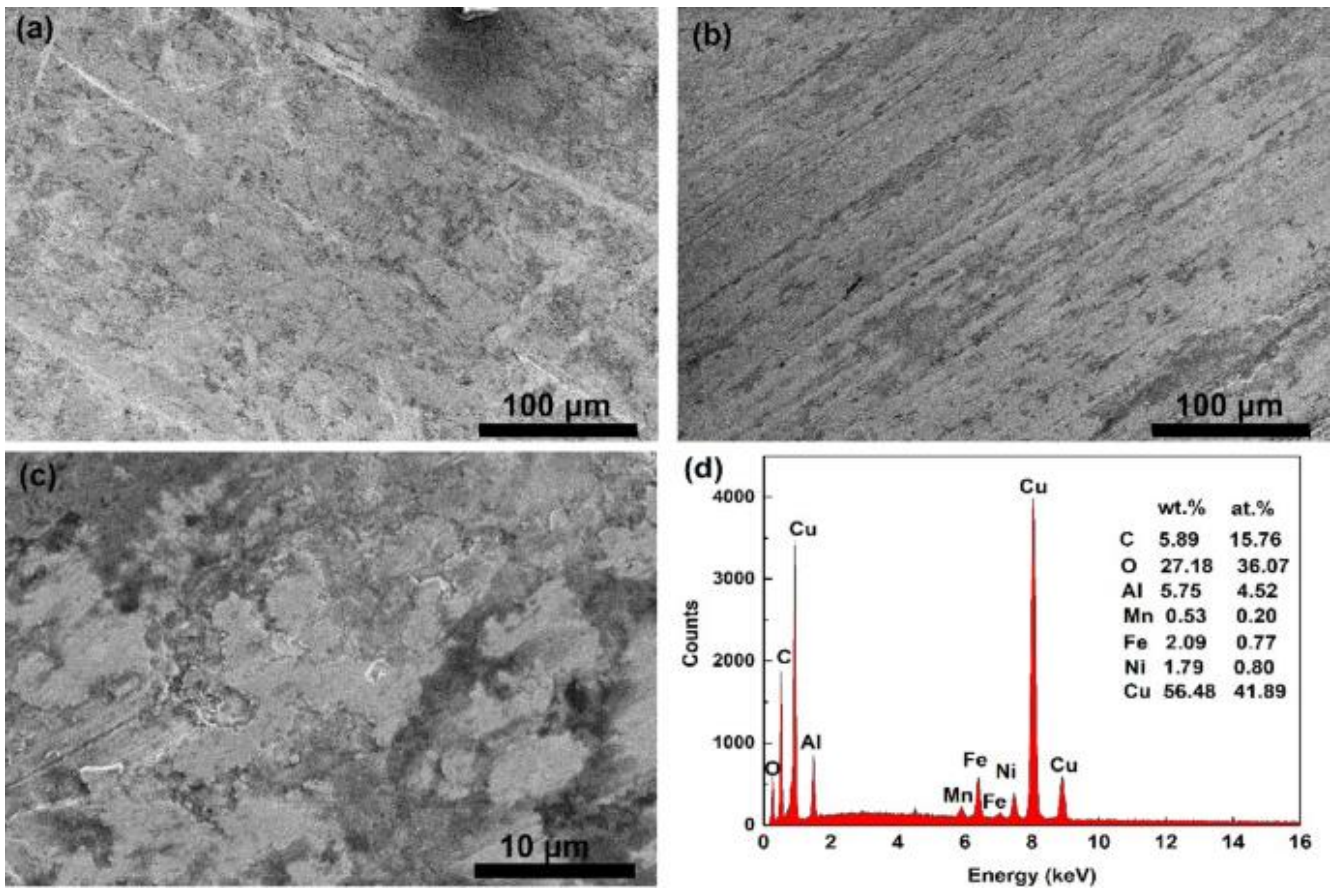
Fig.8 Wear morphologies of the 42CrMo4 counterbodies for **a** EB-PBF and **b** hot-rolled samples at the contact load of 106 N, **c** a high magnification of the wear morphology of the 42CrMo4 counterbody for the EB-PBF sample, **d** EDS result of the transfer layer on the surface of the 42CrMo4 counterbody for the EB-PBF sample
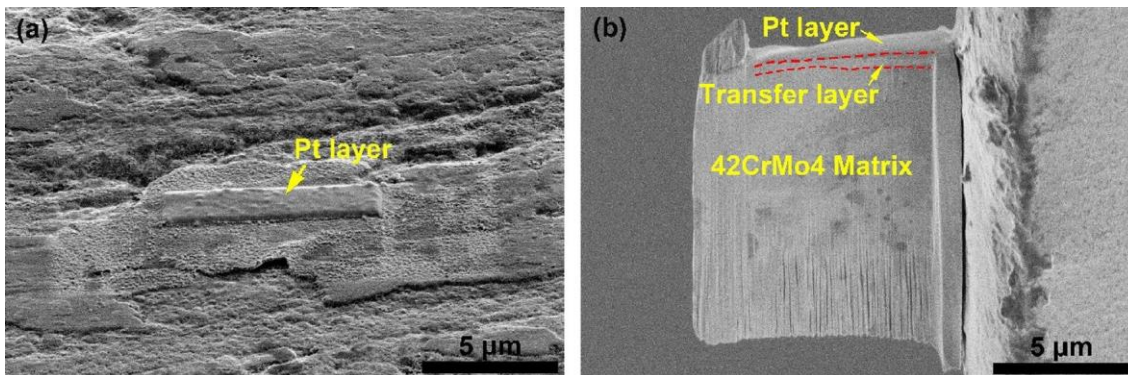
Fig. 9 a Top SEM view of wear surface where FIB was performed on the transfer layer of the surface of 42CrMo4, **b** SEM image of the cross-section showing the transfer layer with a thickness of ~ 0.9 µm
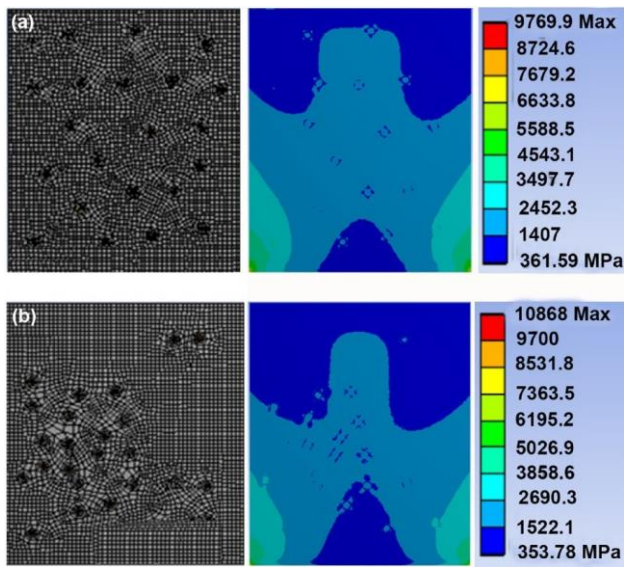
Fig. 10 Finite-element (FE) simulations of the samples with **a** uniform and **b** non-uniformly distributed precipitates after the shear force. Left panels are geometrical configurations for the FE model. Intermediate and right panels show stress distributions at a shear force of 3.75 MPa

4 Discussion

The EB-PBF C63000 alloys shows improved wear resistance compared with the hot-rolled counterparts. In this section, wear and strengthening mechanisms of EB-PBF alloys are discussed from the perspective of matrix strengthening and the formation of a transfer layer.

The strengthening effect from reinforcement, e.g. precipitates has been demonstrated to be effective in the improvement of wear resistance of bulk materials [36]. Precipitates NiAl and Fe$_3$Al are formed in B-PBF C63000 alloys. The wear resistance of EB-PBF C63000 depends on the dimension, distribution and content of precipitates. Grain refinement is also observed after the wear test (Fig. 7). A combination of precipitates and fine grain microstructures further enhances the hardness via precipitation hardening and grain boundary hardening, and thus improves wear resistance.

Additionally, the higher wear resistance of EB-PBF C63000 is related to the uniform distribution of precipitates, which may provide a sustainable work-hardening property. To help understand the effect of uniformly distributed precipitates in the EB-PBF samples, a simulation model was built to estimate the stresses between the uniform and nonuniform cases during the friction process by the finite-element (FE) technique, Fig. 10. The constitutive parameters of the model were based on the experimental

results of C63000 alloys, and shear forces applied in the friction test were used in the modeling. From the FE model, the stress level within C63000 during the friction process was simulated. Various colors represent different stress levels within C63000 during the friction process. The calculation results indicate that the overall stresses in the C63000 alloys with uniformly distributed precipitates are higher than those in the alloys with non-uniformly distributed precipitates (see stress distributions in Fig. 10a, b). This reveals that the uniform distribution of precipitates can effectively promote the local stress concentration during the friction test, and likely help AM parts to obtain high work-hardening performance and thus high hardness with improved wear resistance. These modeling results of the friction case show a sharp contrast with those of the tensile case, where stresses in the uniform precipitation sample were observed to be much lower than those in the non-uniform precipitation sample [30]. This demonstrates that the effect of the precipitate distribution on the internal stress field of the matrix is dependent on the external force direction. For the shear force, the uniformly distributed precipitates promote the overall stress concentration, leading to a higher work-hardening capability of the matrix. The high-stress concentration in AM samples plays a role in improving the wear resistance.

Additionally, the contact surface can be protected by the transfer layer that reduces the shear stress during the wear process. During fretting wear, wear debris would be trapped in the wear interface between NAB and 42CrMo4 surfaces caused by the reciprocating motion with a small displacement amplitude. Oxidation reactions would be occurred with mechanical mixing in the cyclic friction process (Figs. 6 and 7), resulting in the compact transfer layer on the counterbody surface. The transfer layer has been demonstrated to be critical to influence the tribology performance by accommodating interfacial shearing [41]. Thus, the formation of the Cu–O-rich transfer layer with a thickness of ~ 0.9 μm is also responsible for the good tribological behavior of EBPBF C63000.

5 Conclusions

In summary, high wear-resistant NiAl bronze alloys without an increase of friction were successfully prepared by additively manufacturing via electron beam powder bed fusion. The reasons for the enhancement of mechanical properties of EB-PBF processed NAB alloy were the

refinement of microstructures and homogeneously distributed precipitates.

The significantly improved wear resistance, which was two to three times stronger than that of the hot-rolled counterparts, arose from the collective effects including the modulus mismatch between the precipitate and the matrix, the grain refinement in the subsurface, the martensitic transformations around SFs and the formation of the Cu–O-rich transfer layer. This work demonstrated the prospects of the AM technique to produce Cu-based alloys with improved wear resistance combined with high mechanical properties.

References

1. Gao, L.L., Cheng, X.H.: Microstructure and dry sliding wear behavior of Cu–10%Al–4%Fe alloy produced by equal channel angular extrusion. Wear **265**, 986–991 (2008)

2. Li, Z.-H., Cheng, X.-H.: Effects of Equal Channel Angular Extrusion (ECAE) process on the mechanical property and erosion resistance of Ti–5Al–5Mo–5V–3Cr alloy. Tribol. Lett. **62**, 6 (2016)

3. Tang, C.H., Cheng, F.T., Man, H.C.: Effect of laser surface melting on the corrosion and cavitation erosion behaviors of a manganese–nickel–aluminium bronze. Mater. Sci. Eng. A **373**, 195–203 (2004)

4. Azakli, Z., Gümrük, R.: Particle erosion performance of additive manufactured 316L stainless steel materials. Tribol. Lett. **69**, 130 (2021)

5. Thapliyal, S., Dwivedi, D.K.: Study of the effect of friction stir processing of the sliding wear behavior of Cast NiAl Bronze: a statistical analysis. Tribol. Int. **97**, 124–135 (2016)

6. Arab, M., Marashi, S.P.H.: Graphene Nanoplatelet (GNP)incorporated AZ31 magnesium nanocomposite: microstructural, mechanical and tribological properties. Tribol. Lett. **66**, 156 (2018)

7. Han, Y., Wang, L., Liu, K., Yan, W.: Numerical modeling of laser powder bed fusion of metallic glasses: prediction of crystallization. J. Micromech. Mol. Phys. **05**, 2050013 (2021)

8. Yang, H., Wei, L., Lin, X.: A cellular automaton simulation of W-Ni alloy solidification in laser solid forming process. J. Micromech. Mol. Phys. **02**, 1750016 (2018)

9. Herzog, D., Seyda, V., Wycisk, E., Emmelmann, C.: Additive manufacturing of metals. Acta Mater. **117**, 371–392 (2016)

10. Li, Y., Zhou, K., Shu, B.T., Chua, C.K., Leong, K.F.: Heat transfer and phase transition in the selective laser melting process. Int. J. Heat Mass Transf. **108**, 2408–2416 (2017)

11. Liu, J., Stevens, E., Yang, Q., Chmielus, M., To, A.: An analytical model of the melt pool and single track in coaxial laser direct metal deposition (LDMD) additive manufacturing. J. Micromech. Mol. Phys. **02**, 1750013 (2017)

12. Wu, H., Ren, J., Huang, Q., Zai, X., Liu, L., Chen, C., et al.: Effect of laser parameters on microstructure, metallurgical defects and property of AlSi10Mg printed by selective laser melting. J. Micromech. Mol. Phys. **02**, 1750017 (2017)

13. Ai, L., Gao, X.L.: Micromechanical modeling of 3D printable interpenetrating phase composites with tailorable effective elastic properties including negative Poisson's ratio. J. Micromech. Mol. Phys. **02**, 1750015 (2017)

14. DiCecco, L.-A., Mehdi, M., Edrisy, A.: Dry-sliding wear mechanisms of shot-peened additive manufactured alpha titanium featuring TiB particles. Tribol. Lett. **69**, 90 (2021)

15. Jadhav, S., Goossens, L., Kinds, Y., Hooreweder, B., Vanmeensel, K.: Laser-based powder bed fusion additive manufacturing of pure copper. Addit. Manuf. **42**, 101990 (2021)

16. Li, B., Zheng, H., Han, C., Zhou, K.: Nanotwins-containing microstructure and superior mechanical strength of a Cu-9Al5Fe-5Ni alloy additively manufactured by laser metal deposition. Addit. Manuf. **39**, 101825 (2021)

17. Lassègue, P., Salvan, C., De Vito, E., Soulas, R., Herbin, M., Hemberg, A., et al.: Laser Powder Bed Fusion (L-PBF) of Cu and CuCrZr parts: influence of an absorptive Physical Vapor Deposition (PVD) coating on the printing process. Addit. Manuf. **39**, 101888 (2021)

18. Ramirez, D.A., Murr, L.E., Martinez, E., Hernandez, D.H., Martinez, J.L., Machado, B.I., et al.: Novel precipitate–microstructural architecture developed in the fabrication of solid copper components by additive manufacturing using electron beam melting. Acta Mater. **59**, 4088–4099 (2011)

19. Popovich, A., Sufiiarov, V., Polozov, I., Borisov, E., Masaylo, D., Orlov, A.: Microstructure and mechanical properties of additive manufactured copper alloy. Mater. Lett. **179**, 38–41 (2016)

20. Sciammarella, F.M., Gonser, M., Styrcula, M.: Laser Additive Manufacturing of Pure Copper. RAPID, pp. 1241–1248. Place (2013)

21. Liu, Y., Ye, Z., Wang, X., Liang, B., Zhang, Y.: Microstructure and mechanical behavior of Cu–9Al–4Ni-3.5Fe-0.5Mn alloy fabricated by laser melting deposition. Mater. Sci. Eng. A **826**, 142006 (2021)

22. Alkelae, F., Sasaki, S.: Tribological and mechanical characterization of Nickel Aluminium Bronze (NAB) manufactured by Laser Powder-Bed Fusion (L-PBF). Tribology **15**, 126–135 (2020)

23. Zhang, P., Lu, W., Liu, X., Zhou, M., Zhai, W., Zhang, G., et al.: Torsional fretting wear behavior of CuNiAl against 42CrMo4 under flat on flat contact. Wear **380**, 6–14 (2017)

24. Zhai, W., Lu, W., Zhang, P., Zhou, M., Liu, X., Zhou, L.: Microstructure, mechanical and tribological properties of nickel-aluminium bronze alloys developed via gas-atomization and spark plasma sintering. Mater. Sci. Eng. A **707**, 325–336 (2017)

25. Lu, W., Zhai, W., Zhang, P., Zhou, M., Liu, X., Zhou, L.: Effect of different levels of free water in oil on the fretting wear of nickelaluminum bronze based composites. Wear **390–391**, 376–384 (2017)

26. Zhang, P., Liu, X., Lu, W., Zhai, W., Zhou, M., Wang, J.: Fretting wear behavior of CuNiAl against 42CrMo4 under different lubrication conditions. Tribol. Int. **117**, 59–67 (2018)

27. Zhang, P., Lu, W., Liu, X., Zhai, W., Zhou, M., Jiang, X.: A comparative study on torsional fretting and torsional sliding wear of CuNiAl under different lubricated conditions. Tribol. Int. **117**, 78–86 (2018)

28. Zhang, P., Lu, W., Liu, X., Zhai, W., Zhou, M., Zeng, W.: Torsional fretting and torsional sliding wear behaviors of CuNiAl against 42CrMo4 under dry condition. Tribol. Int. **118**, 11–19 (2018)

29. Zhou, M., Lu, W., Liu, X., Zhai, W., Zhang, P., Zhang, G.: Fretting wear properties of plasma-sprayed Ti3SiC2 coatings with oxidative crack-healing feature. Tribol. Int. **118**, 196–207 (2018)

30. Lu, W., Zhai, W., Wang, J., Liu, X., Zhou, L., Ibrahim, A.M.M., et al.: Additive manufacturing of isotropic-grained, high-strength and high-ductility copper alloys. Addit. Manuf. **38**, 101751 (2021)

31. Gourlay, C.M., Dahle, A.K.: Dilatant shear bands in solidifying metals. Nature **445**, 70–73 (2007)

32. Martin, J.H., Yahata, B.D., Hundley, J.M., Mayer, J.A., Schaedler, T.A., Pollock, T.M.: 3D printing of high-strength aluminium alloys. Nature **549**, 365 (2017)

33. Li, P., Li, S.X., Wang, Z.G., Zhang, Z.F.: Unified factor controlling the dislocation evolution of fatigued face-centered cubic crystals. Acta Mater. **129**, 98–111 (2017)

34. Agnew, S.R., Horton, J.A., Yoo, M.H.: Transmission electron microscopy investigation of $\langle c + a \rangle$ dislocations in Mg and α-solid solution Mg-Li alloys. Metall. Mater. Trans. A. **33**, 851–858 (2002)

35. Li, B., Yan, P.F., Sui, M.L., Ma, E.: Transmission electron microscopy study of stacking faults and their interaction with pyramidal dislocations in deformed Mg. Acta Mater. **58**, 173–179 (2010)

36. Zhai, W., Bai, L., Zhou, R., Fan, X., Kang, G., Liu, Y., et al.: Recent progress on wear-resistant materials: designs, properties, and applications. Adv. Sci. 2003739 (2021)

37. Chen, X., Han, Z., Lu, K.: Enhancing wear resistance of Cu–Al alloy by controlling subsurface dynamic recrystallization. Scripta Mater. **101**, 76–79 (2015)

38. Sander, J., Hufenbach, J., Giebeler, L., Bleckmann, M., Eckert, J., Kühn, U.: Microstructure, mechanical behavior, and wear properties of FeCrMoVC steel prepared by selective laser melting and casting. Scripta Mater. **126**, 41–44 (2017)

39. Seol, J.B., Kim, J.G., Na, S.H., Park, C.G., Kim, H.S.: Deformation rate controls atomic-scale dynamic strain aging and phase transformation in high Mn TRIP steels. Acta Mater. **131**, 187–196 (2017)

40. Karewar, S., Sietsma, J., Santofimia, M.J.: Effect of pre-existing defects in the parent fcc phase on atomistic mechanisms during the martensitic transformation in pure Fe: a molecular dynamics study. Acta Mater. **142**, 71–81 (2018)

41. Fischer, A., Dudzinski, W., Gleising, B., Stemmer, P.: Analyzing mild- and ultra-mild sliding wear of metallic materials by transmission electron microscopy. In: Dienwiebel, M., De Barros Bouchet, M.-I. (eds.) Advanced Analytical Methods in Tribology, pp. 29–59. Springer, New York (2018)